ChemPhysMater 3 (2024) 94–102

Contents lists available at ScienceDirect

ChemPhysMater

journal homepage: https://www.keaipublishing.com/en/journals/chemphysmater/

Research Article

Carbon nanotube-supported mixed-valence Mn_3O_4 electrodes for high-performance lithium-oxygen batteries

Yuting Zhu, Jing Gao, Zhongxiao Wang, Rui Sun, Longwei Yin, Chengxiang Wang, Zhiwei Zhang*

Key Laboratory for Liquid-Solid Structural Evolution and Processing of Materials, Ministry of Education, School of Materials Science and Engineering, Shandong University, Jinan 250061, China

ARTICLE INFO

Keywords:
Mixed-valence states
Carbon nanotube
Electrode reaction kinetics
Lithium–oxygen batteries

ABSTRACT

Lithium–oxygen batteries (LOBs) have extensive applications because of their ultra-high energy densities. However, the practical application of LOBs is limited by several factors, such as a high overpotential, poor cycle stability, and limited rate capacity. In this paper, we describe the successful uniform loading of Mn_3O_4 nanoparticles onto multi-walled carbon nanotubes (Mn_3O_4@CNT). CNTs form a conductive network and expose numerous catalytically active sites, and the one-dimensional porous structure provides a convenient channel for the transmission of Li^+ and O_2 in LOBs. The electronic conductivity and electrocatalytic activity of Mn_3O_4@CNT are significantly better than those of MnO@CNT because of the inherent driving force facilitating charge transfer between different valence metal ions. Therefore, the Mn_3O_4@CNT cathode obtains a low overpotential (0.76 V at a limited capacity of 1000 mAh g^{-1}), high initial discharge capacity (16895 mAh g^{-1} at 200 mA g^{-1}), and long cycle life (97 cycles at 200 mA g^{-1}). This study provides evidence that transition metal oxides with mixed-valence states are suitable for application as efficient cathodes for LOBs.

1. Introduction

To meet the increasing energy demands of modern society, it is particularly important to develop rechargeable batteries that have a long battery life and can be used in large electrical equipment such as new energy vehicles [1]. Recently, LOBs have received significant attention owing to their ultra-high theoretical energy density (~3500 Wh kg^{-1}, close to that of gasoline) [2].Generally, lithium peroxide is the main discharge product, and its reversible formation and decomposition ($O_2 + 2Li^+ + 2e^- \leftrightarrow Li_2O_2$) during the oxygen reduction reaction (ORR) and oxygen evolution reaction (OER) are the main source of capacity contribution [2–4]. However, the insulating property of Li_2O_2 and its insolubility in electrolytes leads to slow electrode reaction kinetics, poor rate performance, and inadequate cycle stability, resulting in severe side reactions [4]. Therefore, the rational design of high-efficiency cathode catalysts that can accelerate electrode reaction kinetics and avoid passivation and side reactions is particularly important for fabricating ideal LOBs.

Noble metals (Pt, Ir, etc.) have been recognized as the optimal cathode catalysts because of their excellent catalytic effect on the ORR and OER [5,6]; however, their high price limits their practical application. In contrast, transition metals and transition metal compounds, such as manganese-, chromium-, and cobalt-based compounds, have been well developed because of their low cost and desirable catalytic activity [7–16]. Notably, Cr_2O_3 exhibits good OER catalytic activity owing to the mixed-valence states on the surface [14–17]. Yao et al. reported that the excellent OER catalytic activity of Cr_2O_3 benefited from the solid-state activation process at the Li_2O_2/Cr_2O_3 interface. Furthermore, manganese oxides have attracted increasing attention owing to their excellent chemical stability, environmental compatibility, and abundant natural reserves [9–13]. The oxidation states and crystal structures of manganese oxides are extremely diverse and tunable, providing promising pathways to improve their electrocatalytic activity. Bent et al. demonstrated that MnO (II) and Mn_2O_3 (III) display similar catalytic activity for the OER [12]. However, Mn^{3+} exhibits a significant Jahn-Teller effect, which reduces the stability of the battery during cycling; in contrast, MnO displays better cycling stability [13]. Reports focusing on the application of Mn_3O_4 with mixed-valence states (+3 and +2) for LOBs are scarce.

Generally, pure carbon materials are used as cathodes because of their good electrical conductivity and ORR catalytic activity. However, LOBs comprising pure carbon materials as cathodes have a high charge overpotential and premature cathode passivation, which are due to the slow OER kinetics of carbon [18–20]. Notably, carbon ma-

* Corresponding author.
E-mail address: zhangzhiwei@sdu.edu.cn (Z. Zhang).

https://doi.org/10.1016/j.chphma.2023.03.002
Received 4 February 2023; Received in revised form 12 March 2023; Accepted 12 March 2023
Available online 30 March 2023

terials are commonly employed as substrates to support high OER catalytic active species to prepare high-performance bifunctional catalysts. The synergistic effect between the different components effectively improves the electrocatalytic activity, thereby reducing the charge–discharge overpotential and improving the cycle stability of the LOBs [21–27].

In this study, we synthesized Mn_3O_4 nanoparticle-loaded multiwalled carbon nanotube (Mn_3O_4@CNT) composites, which were used as cathodes for LOBs, using a simple room temperature (25 °C) redox and protective atmosphere annealing method. On the one hand, the inherent one-dimensional (1D) tubular structure of CNTs provides adequate space for accommodating Li_2O_2 to achieve a high discharge specific capacity and supplies convenient channels for the transmission of the electrolyte, electrons (e^-), Li^+, and O_2. Additionally, the large specific surface area of the CNTs facilitates the exposure of abundant active sites [19–22]. During material synthesis, CNTs act as ORR catalytic activators and build a complete conductive skeleton, linking the catalytic material–Mn_3O_4 nanoparticles together, thereby further improving the performance of LOBs. On the other hand, the metal ions on the surface of Mn_3O_4 can be activated by recombining with CNTs [20,23] such that Mn_3O_4 can promote the decomposition of Li_2O_2 through a solid-state activation process similar to that of Cr_2O_3, thereby enhancing the OER catalytic activity. In addition, CNT wrapped with Mn_3O_4 particles can reduce the contact of Li_2O_2 with C, thereby reducing the amount of by-product Li_2CO_3 and improving the cycling stability of the batteries. The results show that the Mn_3O_4@CNT nanocomposites can effectively improve the electrode reaction kinetics, exhibit good OER activity, and display an excellent electrochemical performance [20,23,25]. The LOBs based on Mn_3O_4@CNT exhibit an excellent discharge capacity of 16895 mAh g^{-1}, a low charge–discharge overpotential of 0.76 V at a limited capacity of 1000 mAh g^{-1} (the overpotential of MnO@CNT is 1.31 V under the same conditions), and a cycle life over 90 cycles at 200 mA g^{-1}.

2. Experimental

2.1. Material synthesis

CNTs were pretreated via acidification to remove metal impurities and introduce oxygen-containing functional groups. Pristine CNTs (diameter: < 8 nm, length: 10–30 μm, J&K Scientific) were refluxed in a mixed solution of 10 mL 65 wt% HNO_3 and 30 mL 98 wt% H_2SO_4 at 70 °C for 30 min [28]. Fig. S1 (Supporting Information) shows the specific synthesis steps involved in producing the Mn_3O_4@CNT sample.

Acidified CNTs (0.05 g) were dispersed in 40 mL of deionized water and subjected to ultrasonic treatment for 60 min. Subsequently, $KMnO_4$ (0.15 g) was added to the above-mentioned solution at room temperature (25 °C), and the mixture was magnetically stirred for 12 h. Thereafter, the dark brown particles were centrifuged and washed thrice with deionized water and ethanol. The black precipitates were collected and dried for 12 h in a vacuum oven at 60 °C to obtain the calcined precursor powders. Finally, the precursors were annealed at 500 °C for 3 h in a tube furnace (under Ar gas protection) to obtain the final product, Mn_3O_4@CNT. Similarly, the annealing temperature was set to 900 °C to obtain the comparative MnO@CNT sample.

2.2. Characterizations

The crystallographic information of the samples and discharge product was obtained via powder X-ray diffraction (XRD) on a Rigaku D/Max-KA diffractometer using Cu Kα radiation (λ = 1.5406 Å) with a step size of 0.02° with a dwelling time of 0.5 s. The morphology and microstructure were identified using an SU-70 field emission scanning electron microscope and high-resolution transmission electron microscopy (HRTEM) performed with a JEM-2100 microscope at an acceleration voltage of 200 kV. A thermogravimetric analyzer (TGA1 METTLER TOLEDO) was used for thermogravimetric analysis (TGA) to analyze the compositional changes of the samples from room temperature to 800 °C under air at a heating rate of 10 °C min^{-1}. The surface chemistry was investigated via X-ray photoelectron spectroscopy (XPS) using an ESCALAB 250 spectrometer with a 150 W Al Kα probe beam. The specific surface area and pore size distribution of the materials were measured using nitrogen adsorption–desorption isotherms using a BJ builder Kubo X1000 at −196.15 °C.

2.3. Electrochemical measurements

The cathode material was fabricated from a homogeneous slurry of 70% active material, 20% Super P, and 10% polyvinylidene fluoride (PVDF) dissolved in N-methylpyrrolidone (NMP), to test the electrochemical performance. The slurry was sprayed onto the surface of the carbon paper with a mass load of ~ 0.4 mg cm^{-2}, and the working electrode was obtained after drying at 80 °C for 1 d The model 2032 button cells (19 holes on the cathode side) were assembled in a glove box filled with argon ($H_2O < 0.1 \times 10^{-6}$; $O_2 < 0.1 \times 10^{-6}$); lithium foil was used as the anode; a glass fiber separator (Whatman, GF/D) as the separator; and 1 M LiTFSI dissolved in TEGDME was employed as the electrolyte. All measurements were performed under a 1.0 bar dry O_2 atmosphere (> 99.999%) to avoid the negative impact of the gas impurities in air. Galvanostatic charge–discharge curves were obtained in the voltage window of 2.0–4.5 V on a LAND CT2001A battery system (Wuhan, China). Cyclic voltammetry (CV) and electrochemical impedance spectroscopy (EIS) analyses were performed on an electrochemical workstation (PARSTAT2273). All the electrochemical performance tests were conducted at room temperature.

3. Results and discussion

XRD patterns were obtained to determine the crystal structure and crystallinity of the prepared samples. As shown in Fig. 1(a), the diffraction peaks centered at 18.0°, 28.9°, 31.0°, 32.3°, 36.0°, 44.3°, 53.8°, 59.9°, and 64.7° correspond to the (101), (112), (200), (103), (211), (220), (312), (224), and (314) planes of Mn_3O_4 (PDF#18–0803), respectively, confirming the good crystallinity of Mn_3O_4 derived from Mn_3O_4@CNT. In the XRD patterns of MnO@CNT samples, the peaks located at 34.9°, 40.5°, 58.7°, 70.1°, and 73.8° correspond to the (111), (200), (220), (311), and (222) crystal planes of MnO (PDF#07–0230). The peak at approximately 26° is a typical CNT peak. The intensities of the peaks obtained from the experimental and comparative samples is clearly weaker than those obtained from pure CNT–this phenomenon may be caused by the large quantity of Mn_3O_4 and the MnO coating [23].

TGA (Fig. S2(a)) revealed that the mass percentage of Mn_3O_4 nanoparticles in Mn_3O_4@CNT is approximately 27 wt%. Although the remaining mass of MnO@CNT is 42%, MnO will be converted into Mn_3O_4 at 800 °C, simultaneously, assuming that the amount of adsorbed water is 3%, that is, consistent with that in Mn_3O_4@CNT. Therefore, the actual provisioning mass percentage of MnO in MnO@CNT is only 36 wt% [26–28]. The main reason for the mass fraction of MnO being slightly higher than that of Mn_3O_4 is that more amount of C is consumed via calcination at 900 °C [14,29]. The N_2 desorption and adsorption isotherms illustrate the difference in the pore size and specific surface area of Mn_3O_4@CNT and MnO@CNT in Figs. 1(b) and S2(b). Both materials exhibit a distinct mesoporous structure; as expected, the specific surface area of MnO@CNT (61.427 m^2 g^{-1}) is slightly smaller than that of Mn_3O_4@CNT (69.15 m^2 g^{-1}), owing to the high-temperature annealing at 900 °C, which causes small grains to aggregate into large grains [26,30]. The large specific surface area can accelerate the transmission of e^-, O_2, and Li^+ and expose numerous catalytic active sites to promote the ORR/OER process. In addition, the large specific surface area can provide more space to accommodate larger amounts of Li_2O_2 during discharge and ensure a high discharge specific capacity [14,31].

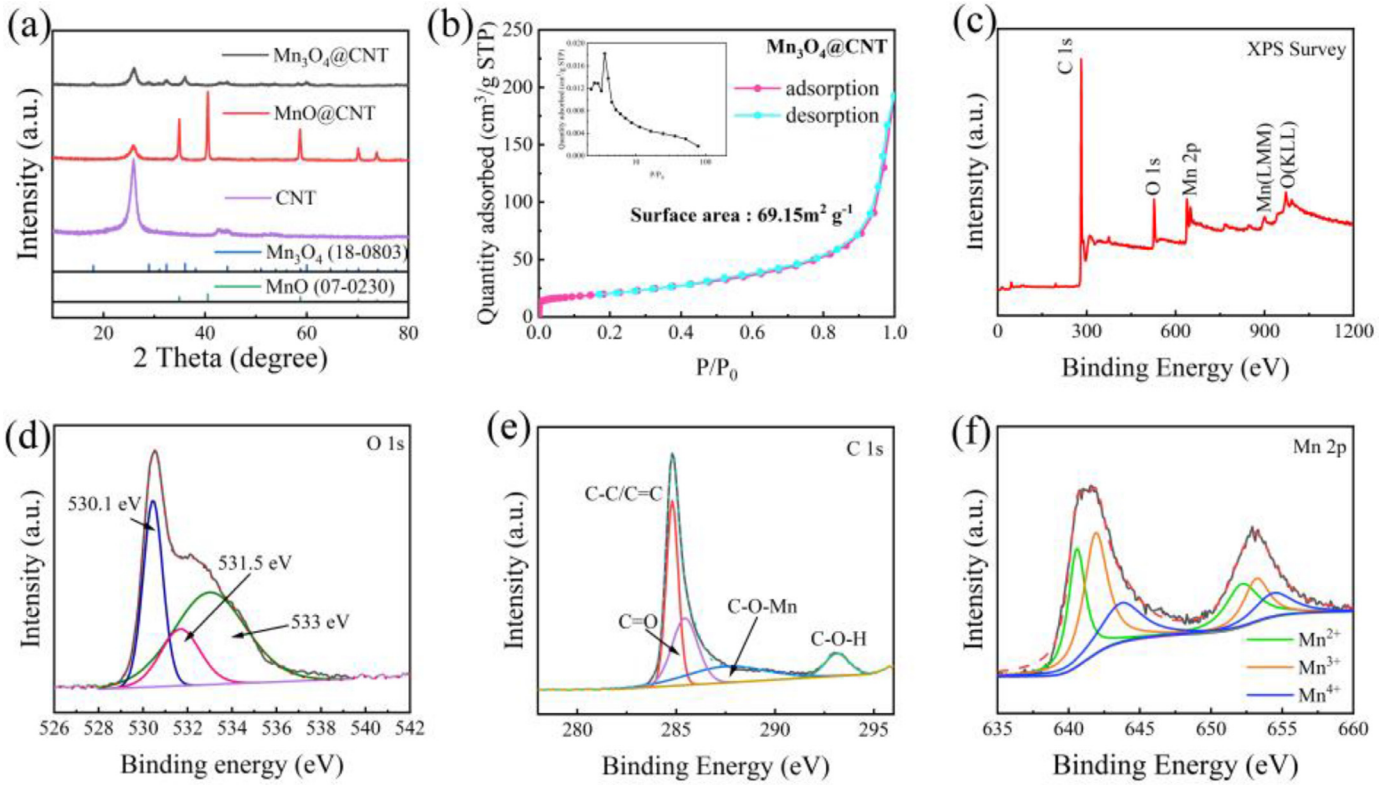

Fig. 1. (a) XRD patterns of Mn_3O_4@CNT, MnO@CNT, and CNT; (b) N_2 adsorption and desorption isotherms and pore size distribution curves (inset) of Mn_3O_4@CNT; (c) XPS survey spectra and high-resolution XPS spectra of (d) O 1s, (e) C 1s, and (f) Mn 2p of Mn_3O_4@CNT.

XPS was used to analyze the elemental chemical bonding state and composition [32].

Fig. 1(c) shows the survey spectrum of Mn_3O_4@CNT and clearly indicates the existence of the Mn, C, and O elements. The O 1s high-resolution spectrum is fitted to three peaks at 530.1, 531.5, and 533 eV (Fig. 1(d)), which are related to lattice oxygen, oxygen defects, and adsorbed water, respectively. The presence of defective oxygen improves the electrocatalytic activity [33,34]. The C 1s pattern could be split into four peaks (Fig. 1(e)): the peak at approximately 284.7 eV originates from the C=C or C–C bonds in CNTs, and the other three peaks centered at 285.1, 287.1, and 293.3 eV are assigned to the C=O, C–O–Mn, and C–O–H, which are introduced after high-temperature calcination. Therefore, it can be concluded that Mn_3O_4 and CNTs are connected by bonding rather than physical adsorption [32].

Fig. 1(f) shows the fine spectrum of Mn 2p; the two characteristic peaks at 642.4 and 653.6 eV correspond to Mn 2p3/2 and Mn 2p1/2, respectively. Peak deconvolution revealed that Mn^{2+} (641 and 652.8 eV), Mn^{3+} (642.2 and 653.8 eV), and Mn^{4+} (643.6 and 655 eV) exist in Mn_3O_4@CNT with typical multivalent characteristics. The appearance of Mn^{4+} may be caused by surface oxidation [34–36]. The XPS spectra of MnO@CNT are shown in Fig. S2(c). The fine spectrum of Mn 2p (Fig. S2(f)) in MnO@CNT is well matched with Mn^{3+}, and no other valence states are observed [13].

The scanning electron microscopy (SEM) images of Mn_3O_4@CNT and MnO@CNT are shown in Figs. 2(a) and S3(a), respectively. CNTs are uniform in size, with an outer diameter of approximately 50 nm. The distribution of Mn_3O_4 cannot be clearly observed. Additionally, particle agglomeration is not observed (Fig. 2(a)). In contrast, Fig. S3(a) clearly shows that many small particles are uniformly supported on the CNTs.

TEM characterization was performed to further understand the microstructures of the samples.

From Figs. 2(b)–(d), Mn_3O_4 nanoparticles with a diameter of approximately 20 nm are uniformly anchored on the CNTs. The TEM image of MnO@CNT, shown in Fig. S3(b), indicates that the particle size distribution of MnO is between 80 and 150 nm. This is because small grains agglomerate and grow into large grains owing to the high temperature of 900 °C. Specifically, the reduction in the average particle size can shorten the ion diffusion path, accelerate the ion diffusion process, reduce the volume expansion of particles, and prevent the particles from being damaged [26].

The HRTEM images in Figs. 2(e) and S3(c) show discernible lattice fringes indicating the perfect crystalline structures of Mn_3O_4@CNT and MnO@CNT, respectively. On the one hand, the crystal plane spacings of 0.276 and 0.492 nm in Fig. 2(e) can be assigned to the (112) and (101) planes of Mn_3O_4 [37,38]. On the other hand, in Fig. S3(c), the interlinear distance between lattice fringes is 0.224 nm, corresponding to the (200) crystal plane of MnO [39]. The selected area electron diffraction (SAED) patterns in Figs. 2(f) and S3(d) also confirm the production of manganese-based oxides. This is consistent with the description obtained from the XRD [39,40].

Mn_3O_4@CNT and MnO@CNT were applied as bifunctional catalytic cathodes for nonaqueous LOBs to estimate the electrocatalytic activity of the prepared samples. As a blank control, CNTs were used as a cathode to assemble the battery. CV analysis was performed at a voltage window of 2.0–4.5 V and a scan rate of 0.1 mV s^{-1} to evaluate the electrocatalytic performance of Mn_3O_4@CNT, MnO@CNT, and CNT (Fig. 3(a)).

All three cathodes display conspicuous reduction peaks during the discharge process owing to the production of Li_2O_2 ($O_2 + 2Li^+ + 2e^- \rightarrow Li_2O_2$). However, Mn_3O_4@CNT has a larger ORR peak area than the MnO@CNT and CNT electrodes, that is, Mn_3O_4@CNT may produce more Li_2O_2 [41]. Notably, in addition to the distinct oxidation peak appearing after 4 V, the Mn_3O_4@CNT composite electrode exhibits another oxidation peak at approximately 3.4 V during charging. The additional oxidation peak corresponds to the stepwise reversible decomposition process of Li_2O_2 ($Li_2O_2 \rightarrow O_2 + 2Li^+ + 2e^-$), which also indicates that Mn_3O_4@CNT has faster OER catalytic kinet-

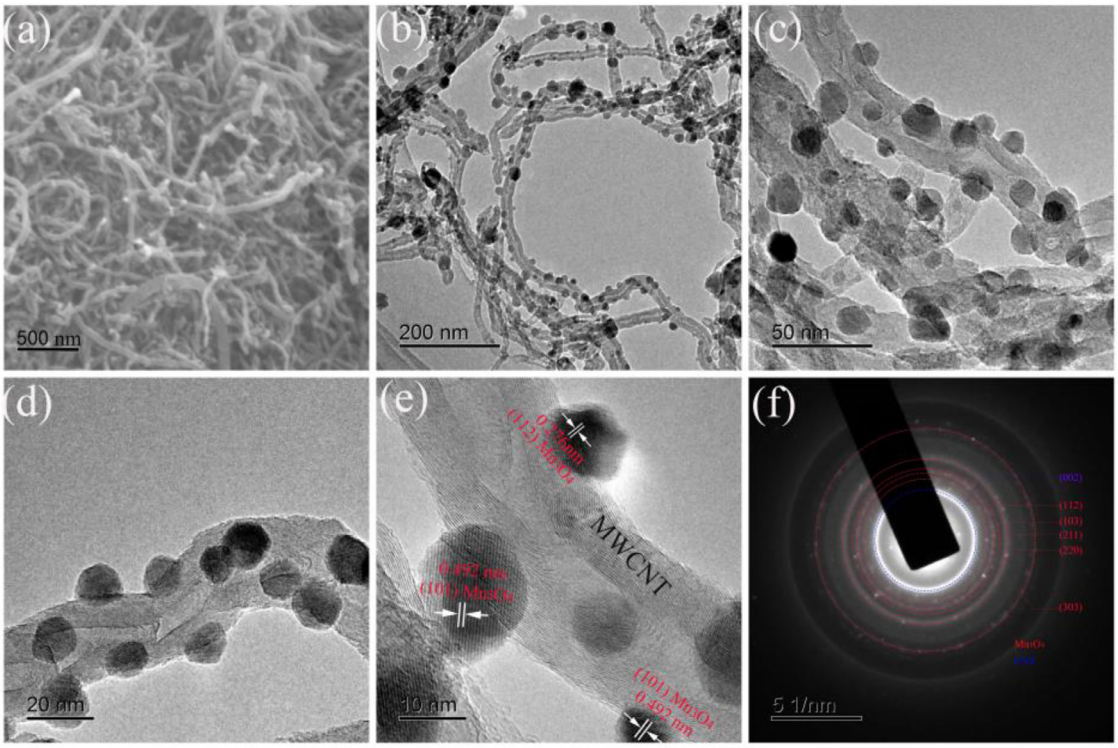

Fig. 2. (a) SEM images of Mn_3O_4@CNT; (b)–(d) TEM images of Mn_3O_4@CNT with different magnifications; (e) HRTEM images and (f) SAED patterns of Mn_3O_4@CNT.

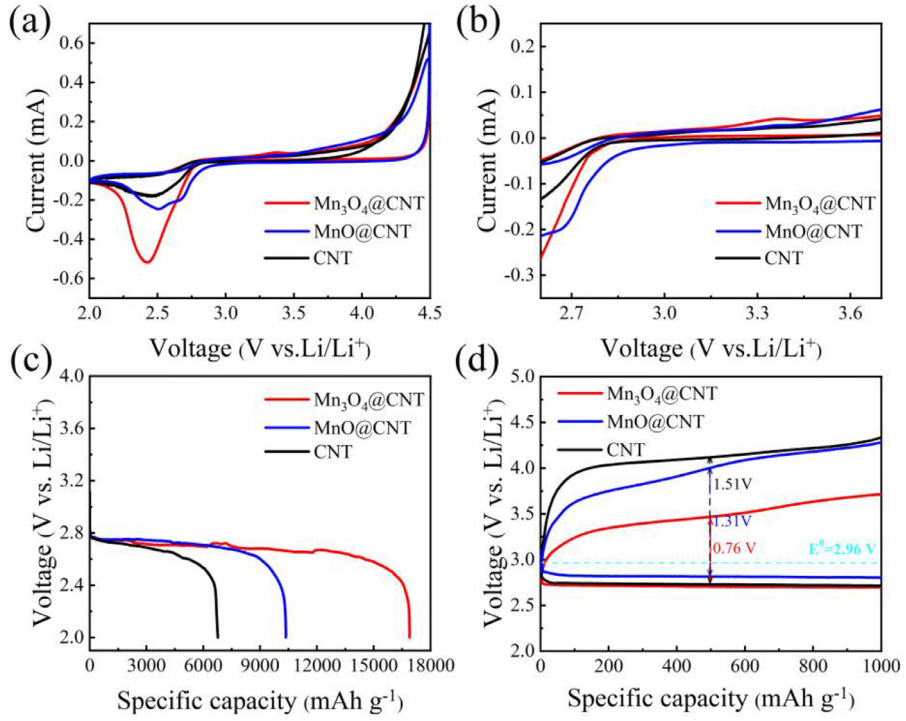

Fig. 3. (a) CV curves of Mn_3O_4@CNT, MnO@CNT, and CNT cathodes within a voltage window of 2.0–4.5 V at a scan rate of 0.1 mV s^{-1}. (b) Enlarged CV curves of Mn_3O_4@CNT, MnO@CNT, and CNT electrodes within a voltage window of 2.6–3.7 V. (c) Initial discharge capacity curves of Mn_3O_4@CNT, MnO@CNT, and CNT electrodes at 200 mA g^{-1}. (d) Discharge–charge curves of Mn_3O_4@CNT, MnO@CNT, and CNT electrodes with a limited capacity of 1000 mAh g^{-1} at 200 mA g^{-1}.

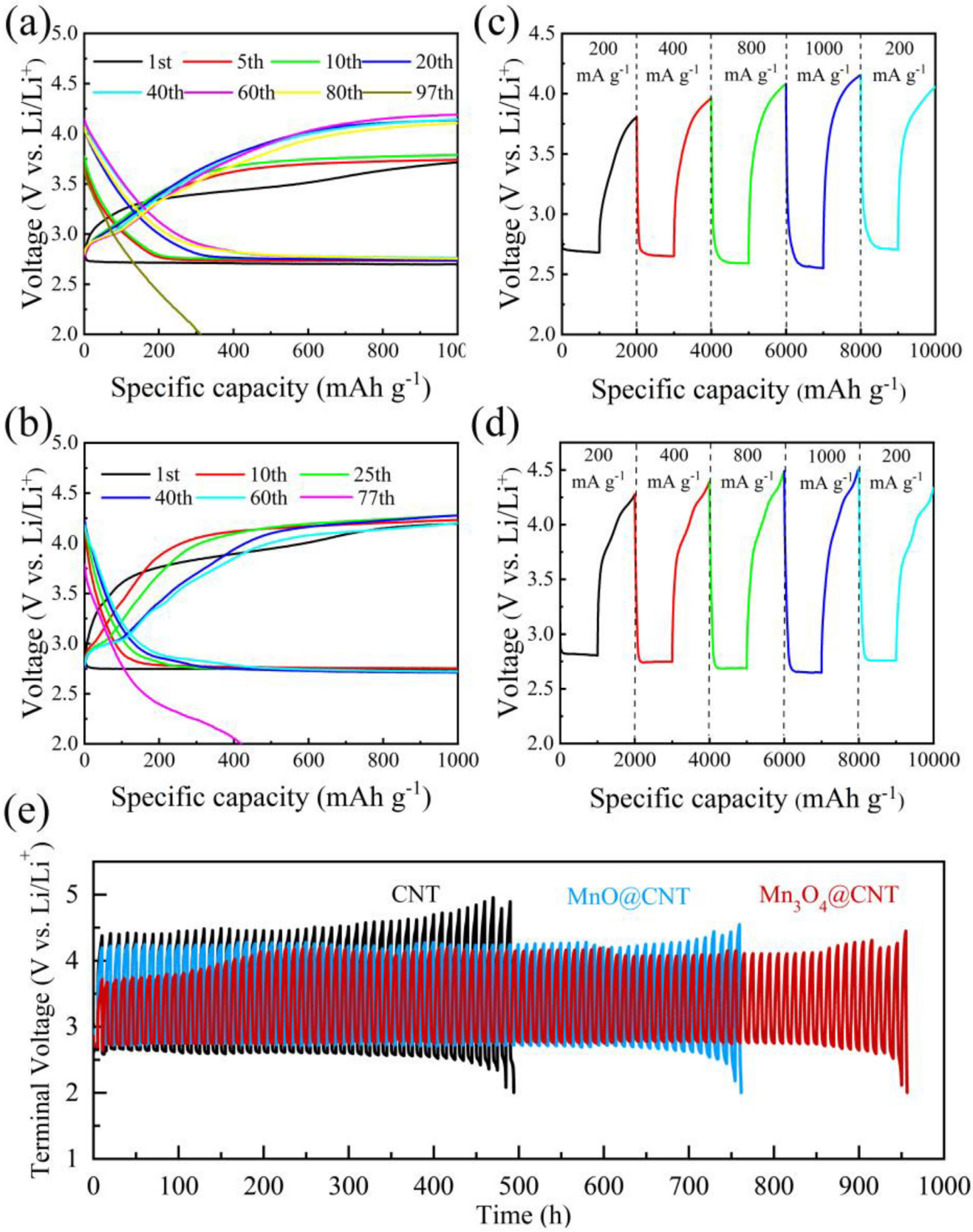

Fig. 4. Discharge–charge profiles of (a)(b) Mn_3O_4@CNT and MnO@CNT at 200 mA g^{-1} with different cycles; discharge–charge profiles of (c)(d) Mn_3O_4@CNT and MnO@CNT electrodes with a limited capacity of 1000 mAh g^{-1} at different current densities ranging from 200 to 1000 mA g^{-1}; (e) cycling performance comparison of CNT, MnO@CNT, and Mn_3O_4@CNT cathodes at 200 mA g^{-1} with a fixed capacity of 1000 mAh g^{-1}.

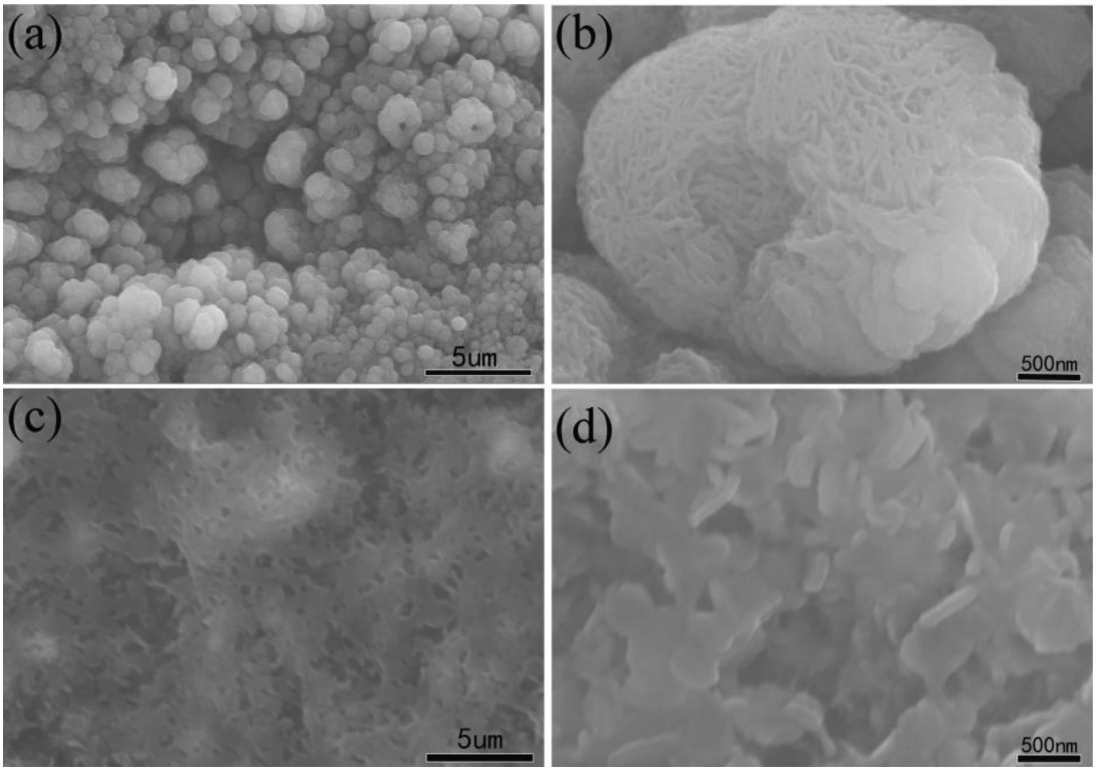

Fig. 5. Ex-situ SEM images of fully discharged (a)(b) Mn_3O_4@CNT and (c)(d) MnO@CNT electrodes.

ics than MnO@CNT and CNTs [42,43]. Fig. 3(b) is a partially enlarged view of Fig. 3(a) and clearly displays the redox onset potentials of the three materials. Fig. 3(c) shows the complete discharge curves of the three cathodes with a cut-off voltage of 2 V at a current density of 200 mA g^{-1}. The Mn_3O_4@CNT electrode has the highest initial discharge specific capacity (16895 mAh g^{-1}), followed by the MnO@CNT electrode (10360 mAh g^{-1}). The CNT electrode has the lowest (6770 mAh g^{-1}) initial discharge specific capacity. These findings correspond with the CV analysis results. The ORR overpotential of the MnO@CNT electrode is slightly lower than that of the Mn_3O_4@CNT electrode during the early period of full discharge (before 6000 mAh g^{-1}), which may be caused by the larger number of exposed C sites in MnO@CNT. However, the ORR catalytic activity of the Mn_3O_4@CNT electrode is better than that of MnO@CNT during deep discharge, which may be because of the rapid passivation on the surface of MnO@CNT. LOBs comprising a Mn_3O_4@CNT electrode display a lower overpotential (0.76 V) than those comprising MnO@CNT (1.31 V) and CNT electrodes (1.51 V) at a current density of 200 mA g^{-1} with a cut-off capacity of 1000 mAh g^{-1} (Fig. 3(d)), which indicates the faster kinetics of the electrode reaction.

Additionally, three cathodes were tested with a limited capacity of 1000 mAh g^{-1} at 200 mA g^{-1} to further illustrate the excellent chargeability and cycling stability of the Mn_3O_4@CNT cathode.

Figs. 4(a)(b) and S4(a) show the discharge–charge curves for LOBs with Mn_3O_4@CNT, MnO@CNT, and CNT electrodes at different cycles, respectively. The Mn_3O_4@CNT cathode can cycle stably for 97 cycles when the discharge cut-off voltage and charging cut-off voltage are set to 2.0 and 4.5 V. In contrast, the MnO@CNT and CNT electrodes can only achieve 77 and 50 cycles, respectively, under the same conditions.

Furthermore, LOBs with Mn_3O_4@CNT, MnO@CNT, or CNT cathodes were tested with the same limited capacity (1000 mAh g^{-1}) at different current densities to evaluate their rate capabilities, as shown in Figs. 4(c)(d) and S4(b).

The discharge and charge cut-off voltages of the Mn_3O_4@CNT electrode are 2.69 and 3.80 V at 200 mA g^{-1}, respectively, while the current density increases to 1000 mA g^{-1}; the discharge cut-off voltage gradually decreases to 2.55 V, and the charge cut-off voltage slowly increases to 4.15 V. The charge–discharge voltage exhibits good reversibility when the current density is 200 mA g^{-1}. Therefore, the Mn_3O_4@CNT electrode has an excellent rate capability. In contrast, although the MnO@CNT cathode also has an ideal rate capability, its overpotential is higher at lower current densities. The CNT electrode is extremely unstable at high current densities (800, 1000 mA g^{-1}). Moreover, the Mn_3O_4@CNT cathode has better cycling ability and electrode reaction kinetics than the MnO@CNT and CNT cathodes, as shown in Fig. 4(e).

The discharge products were characterized using ex-situ SEM to reveal the intrinsic mechanism for the excellent electrochemical performance of the Mn_3O_4@CNT composite electrode.

Figs. 5(a)(b) indicate that abundant hairball-shaped discharge products are produced on the Mn_3O_4@CNT electrode after the first discharge. The diameter of the discharge product is approximately 2 μm; the product is tightly and uniformly coated on the surface of the active material and has good interfacial contact with Mn_3O_4@CNT. Such large agglomerates ensure the high discharge capacity of the catalytic cathode. This unique porous structure facilitates the rapid transport of O_2 and Li^+, which promotes the complete decomposition of Li_2O_2 after charging. As expected, the discharge products of the Mn_3O_4@CNT cathode decomposed completely without significant deformation after charging (Fig. S5(a)), illustrating that the Mn_3O_4@CNT electrode exhibits high reversibility and excellent catalytic activity [31,41,44]. In contrast, the discharge products generated on the MnO@CNT cathode surface formed a film, after the first discharge (Figs. 5(c)(d)); therefore, it is easy to passivate the active sites, resulting in limited capacity and earlier death [31]. Additionally, the SEM images of the MnO@CNT cathode, after full recharge (Fig. S5(b)), clearly reveals that certain discharge products remain intact. The continuous accumulation of discharge products on the cathode surface is the main reason for the limited cycle life and poor reversibility.

EIS was performed to further reveal the reversibility of the ORR/OER processes in different charge and discharge states.

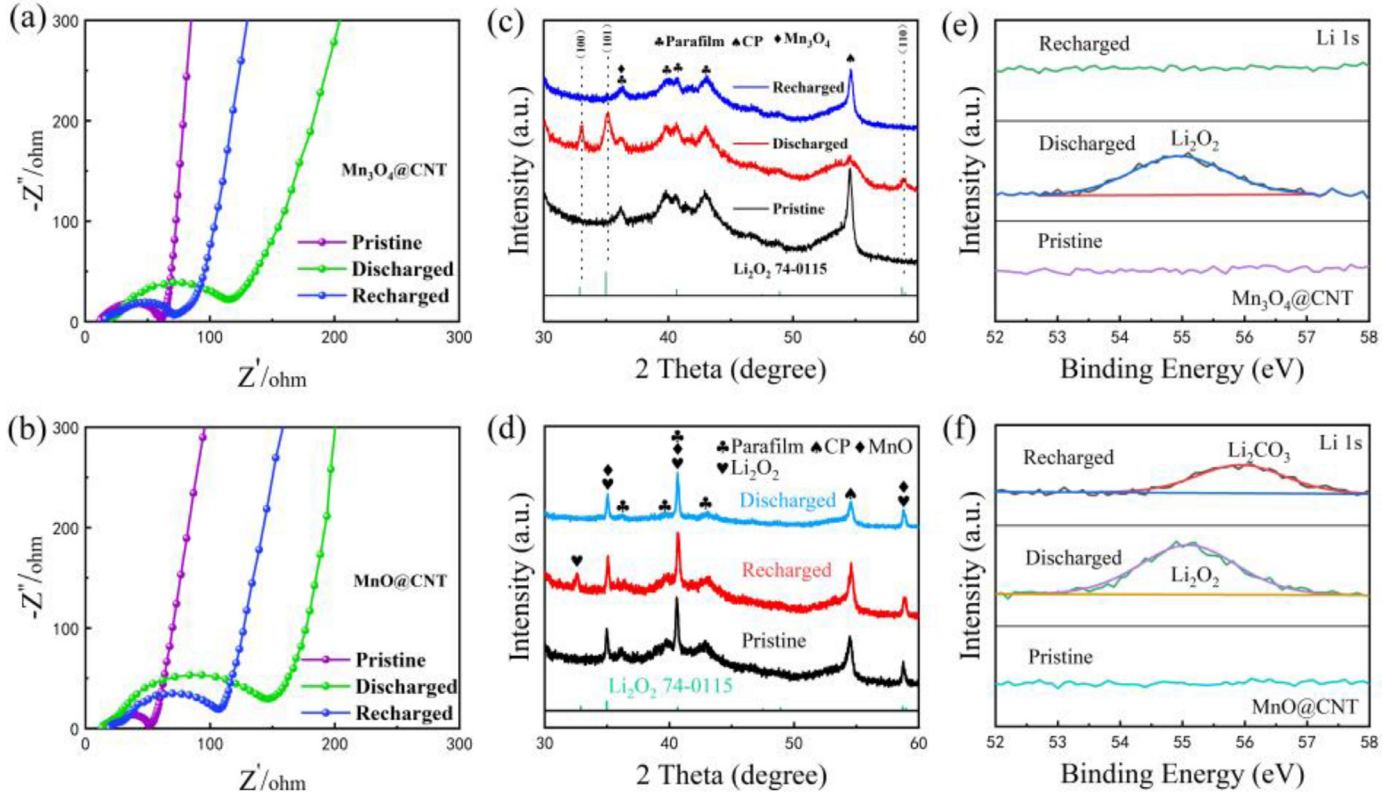

Fig. 6. Nyquist plots of (a) Mn_3O_4@CNT and (b) MnO@CNT at different discharge–charge stages; ex-situ XRD patterns of (c) Mn_3O_4@CNT and (d) MnO@CNT cathodes; ex-situ Li 1s XPS spectrum of pristine, discharged, and recharged (e) Mn_3O_4@CNT and (f) MnO@CNT electrodes.

Fig. S6(a) presents the raw impedance comparison data for the three cathodes. Although Mn_3O_4 and MnO are transition metal oxides, the impedance, after coating on the CNT, does not increase markedly, thereby improving the catalytic activity of the material [45]. As shown in Figs. 6(a)(b) and S6(b), the insulating discharge product covering the electrode surface passivates the active sites and inevitably blocks the charge transport channel, resulting in a notable increase in the charge transfer resistance of all the cathodes after discharge. In contrast, the impedance of the Mn_3O_4@CNT electrode almost returns to its initial state after charging, implying that the Li_2O_2 coated on the surface of the electrode has decomposed [44]. This is consistent with the results obtained from the ex-situ SEM analysis in Fig. S5(a). The impedance of the MnO@CNT and CNT electrodes is significantly higher than the initial value after charging, implying that it is more difficult to decompose Li_2O_2 or that by-products are generated on the surface [31].

The phase composition of the discharge products and reversibility of the cathodes were further studied using XRD.

Figs. 6(c)–(f) show the XRD patterns of the Mn_3O_4@CNT and MnO@CNT electrodes after the first full charge and discharge, respectively. After discharging, the diffraction peaks appearing at 32.8°, 35.4°, and 59° correspond to the (100), (101), and (110) crystal planes of Li_2O_2 (PDF#74–0115), respectively, indicating that the main discharge product of the LOBs is Li_2O_2. The diffraction peaks of Li_2O_2 disappear after charging, indicating that the formation and decomposition of Li_2O_2 are the main sources of the battery capacity [46–48].

The by-products on the Mn_3O_4@CNT and MnO@CNT electrodes were characterized using ex-situ XPS.

As shown in Figs. 6(e)(f), the Li 1s fine spectra of the two cathodes, after discharging, indicate that the main discharge product is Li_2O_2 (54.9 eV). In contrast, for the Mn_3O_4@CNT electrode, the Li_2O_2 is completely decomposed after 15 cycles with a cut-off capacity of 1000 mAh g^{-1}. However, the MnO@CNT electrode displays a typical Li_2CO_3 peak at 55.8 eV under the same conditions, confirming that the Mn_3O_4@CNT cathode has better cycling stability and electrocatalytic activity than MnO@CNT and CNT cathodes [19,49].

We analyzed the Mn 2p fine spectra of the Mn_3O_4@CNT electrode under different states to explore the role of multivalent manganese-based oxides in the ORR and OER processes of LOBs (Fig. S6(c)). In contrast to the case of the Li 1s fine spectrum, in this experiment, the limited capacity is set to 500 mAh g^{-1}, which avoids the generation of copious amounts of Li_2O_2 and the disappearance of the Mn 2p fine spectrum of the electrode, after discharging. Mn 2p3/2 and Mn 2p1/2 peaks shift to 642.5 and 654.2 eV, respectively, after discharging, which indicates the increase in the average valence state of Mn; that is, the e^- required to form Li_2O_2 during the discharge process may partly originate from the conversion of low-valence manganese to high-valence manganese in Mn_3O_4. The Mn 2p spectrum returns to the initial state after charging; this proves the good reversibility of Mn_3O_4@CNT and confirms that the overflowing e^-, during the decomposition of Li_2O_2, are captured by high-valence manganese ions in Mn_3O_4; the high-valence manganese ions are transformed into low-valence manganese ions. Therefore, the inherent electric field formed between Mn ions of different valence states in the Mn_3O_4@CNT electrode is conducive to the transfer of e^- and facilitates the conversion between valence states, thereby improving the electrode reaction kinetics; therefore, the generation and decomposition of Li_2O_2 are ultimately promoted.

4. Conclusions

We prepared Mn_3O_4@CNT and MnO@CNT electrodes with typical core–shell structures by uniformly loading Mn_3O_4 nanoparticles on multi-walled CNTs via a conventional method using room temperature redox and annealing under a protective atmosphere. Owing to the unique mixed-valence metal ions, the Mn_3O_4 nanoparticles coated on the CNT walls could promote the decomposition and deposition of reaction products through the conversion of valence states during

the charge and discharge processes. This phenomenon reduced the discharge and charge overpotential of LOBs, which was demonstrated via ex-situ XPS. The Mn_3O_4@CNT cathode exhibited an excellent electrochemical performance in LOBs, including a low discharge–charge overpotential (0.76 V at a cut-off capacity of 1000 mAh g^{-1}), a high discharge specific capacity (16895 mAh g^{-1} at 200 mA g^{-1}), and an excellent cycle life (more than 90 cycles) under a fixed capacity of 1000 mAh g^{-1} at 200 mA g^{-1}. The marked improvement in the electrochemical performance was attributed to the synergistic effect between the core and shell structures and the rapid e^- transfer among the metal ions.

A conductive network constructed of 1D CNTs can provide convenient O_2 and e^- transfer pathways and adequate space to store Li_2O_2. The inherent charge-transfer driving force originating from metal ions of different valence states facilitates rapid e^- transfer kinetics and ion diffusion during discharge and charge processes. Therefore, the Mn_3O_4@CNT composites prepared in this study are excellent catalysts for LOBs.

Declaration of Competing Interest

The authors declare that they have no known competing financial interests or personal relationships that could have appeared to influence the work reported in this paper.

Acknowledgements

We acknowledge financial support from the Nature Science Foundation of Shandong Province (Grant No: ZR2019BEM019) and Future Plans of Young Scholars at Shandong University.

Supplementary materials

Supplementary material associated with this article can be found, in the online version, at doi:10.1016/j.chphma.2023.03.002.

References

[1] G. Cong, W. Wang, N.C. Lai, Z. Liang, Y.C. Lu, A high-rate and long-life organic–oxygen battery, Nat. Mater. 18 (2019) 390–396.
[2] D. Du, Z. Zhu, K.Y. Chan, F. Li, J. Chen, Photoelectrochemistry of oxygen in rechargeable Li-O_2 batteries, Chem. Soc. Rev. 51 (2022) 1926.
[3] W. Zhou, H. Zhang, H. Nie, Y. Ma, Y. Zhang, H. Zhang, Hierarchical micron-sized mesoporous/macroporous graphene with well-tuned surface oxygen chemistry for high capacity and cycling stability Li-O_2 battery, ACS Appl. Mater. Interfaces 7 (2015) 3389–3397.
[4] A. Débart, A.J. Paterson, J. Bao, P.G. Bruce, α-MnO_2 nanowires: A catalyst for the O_2 electrode in rechargeable lithium batteries, Angew. Chem. Int. Edit. 47 (2008) 4521–4524.
[5] Y. Zhou, K. Yin, Q. Gu, L. Tao, Y. Li, H. Tan, J. Zhou, W. Zhang, H. Li, S. Guo, Lewis-acidic PtIr multipods enable high-performance Li-O_2 batteries, Angew. Chem. Int. Edit. 60 (2021) 26592–26598.
[6] Y.C. Lu, H.A. Gasteiger, Y. Shao-Horn, Catalytic activity trends of oxygen reduction reaction for nonaqueous Li-air batteries, J. Am. Chem. Soc. 133 (2011) 19048–19051.
[7] Y. Zheng, R. Gao, L. Zheng, L. Sun, Z. Hu, X. Liu, Ultrathin Co_3O_4 nanosheets with edge-enriched {111} planes as efficient catalysts for lithium–oxygen batteries, ACS Catal. 9 (2019) 3773–3782.
[8] D. Cao, L. Zheng, Q. Li, J. Zhang, Y. Dong, J. Yue, X. Wang, Y. Bai, G. Tan, C. Wu, Crystal phase-controlled modulation of binary transition metal oxides for highly reversible Li-O_2 batteries, Nano Lett. 21 (2021) 5225–5232.
[9] R. Bi, G. Liu, C. Zeng, X. Wang, L. Zhang, S.Z. Qiao, 3D Hollow α-MnO_2 framework as an efficient electrocatalyst for lithium–oxygen batteries, Small 15 (2019) 1804958.
[10] Y. He, D. Aasen, H. Yu, M. Labbe, D.G. Ivey, J.G. Veinot, Mn_3O_4 nanoparticle-decorated hollow mesoporous carbon spheres as an efficient catalyst for oxygen reduction reaction in Zn–air batteries, Nanoscale Adv. 2 (2020) 3367–3374.
[11] K.R. Yoon, G.Y. Lee, J.W. Jung, N.H. Kim, S.O. Kim, I.D. Kim, One-dimensional RuO_2/Mn_2O_3 hollow architectures as efficient bifunctional catalysts for lithium–oxygen batteries, Nano Lett. 16 (2016) 2076–2083.
[12] K.L. Pickrahn, S.W. Park, Y. Gorlin, H.B.R. Lee, T.F. Jaramillo, S.F. Bent, Active MnO*x* electrocatalysts prepared by atomic layer deposition for oxygen evolution and oxygen reduction reactions, Adv. Energy Mater. 2 (2012) 1269–1277.
[13] W.B. Luo, S.L. Chou, J.Z. Wang, Y.C. Zhai, H.K. Liu, A facile approach to synthesize stable CNTs@MnO electrocatalyst for high energy lithium oxygen batteries, Sci. Rep. 5 (2015) 1–8.
[14] X.Z. Zhang, D. Han, Y.B. He, D.Y. Zhai, D. Liu, H. Du, B. Li, F. Kang, Mesoporous Cr_2O_3 nanotubes as an efficient catalyst for Li-O_2 batteries with low charge potential and enhanced cyclic performance, J. Mater. Chem. A 4 (2016) 7727–7735.
[15] T. Ishihara, I.C. Jang, S. Ida, Preparation of MnO_2-Cr_2O_3 mesoporous oxide and its application for an active and reversible air catalyst for Li-O_2 batteries, Electrochim. Acta 317 (2019) 594–603.
[16] N.C. Lai, G. Cong, Z. Liang, Y.C. Lu, A highly active oxygen evolution catalyst for lithium-oxygen batteries enabled by high-surface-energy facets, Joule 2 (2018) 1511–1521.
[17] K.P. Yao, Y.C. Lu, C.V. Amanchukwu, D.G. Kwabi, M. Risch, J. Zhou, A. Grimaud, P.T. Hammond, F. Bardé, Y. Shao-Horn, The influence of transition metal oxides on the kinetics of Li_2O_2 oxidation in Li-O_2 batteries: High activity of chromium oxides, Phys. Chem. Chem. Phys. 16 (2014) 2297–2304.
[18] T. Zhang, B. Zou, X. Bi, M. Li, J. Wen, F. Huo, K. Amine, J. Lu, Selective growth of a discontinuous subnanometer Pd film on carbon defects for Li-O_2 batteries, ACS Energy Lett. 4 (2019) 2782–2786.
[19] Y.S. Cho, H. Kim, M. Byeon, D.Y. Kim, H. Park, Y. Jung, Y. Bae, M. Kim, D. Lee, J. Park, Enhancing the cycle stability of Li-O_2 batteries via functionalized carbon nanotube-based electrodes, J. Mater. Chem. A 8 (2020) 4263–4273.
[20] W.S. Zhang, Y.T. Liu, G.P. Wu, Surface modification of multiwall carbon nanotubes by electrochemical anodic oxidation, New Carbon Mater. 35 (2020) 155–164.
[21] Y.K. Jo, W. Tamakloe, X. Jin, J. Lim, S.B. Patil, Y.M. Kang, S.J. Hwang, Multilayer hybrid nanosheet of mesoporous carbon–layered metal oxide as a highly efficient electrocatalyst for Li-O_2 batteries, Appl. Catal. B: Environ. 254 (2019) 523–530.
[22] Z.D. Yang, X.Y. Yang, T. Liu, Z.W. Chang, Y.B. Yin, X.B. Zhang, J.M. Yan, Q. Jiang, In situ CVD derived Co–N–C composite as highly efficient cathode for flexible Li-O_2 batteries, Small 14 (2018) 1800590.
[23] D. Li, L. Zhao, Q. Xia, J. Wang, X. Liu, H. Xu, S. Chou, Activating MoS_2 nanoflakes via sulfur defect engineering wrapped on CNTs for stable and efficient Li-O_2 batteries, Adv. Funct. Mater. 32 (2022) 2108153.
[24] Y. Dou, X.G. Wang, D. Wang, Q. Zhang, C. Wang, G. Chen, Y. Wei, Z. Zhou, Tuning the structure and morphology of Li_2O_2 by controlling the crystallinity of catalysts for Li-O_2 batteries, Chem. Eng. J. 409 (2021) 128145.
[25] D.J. Yan, X.D. Zhu, Y.C. Mao, S.Y. Qiu, L.L. Gu, Y.J. Feng, K.N. Sun, Hierarchically organized CNT@TiO_2@Mn_3O_4 nanostructures for enhanced lithium storage performance, J. Mater. Chem. A 5 (2017) 17048–17055.
[26] W. Mao, W. Yue, Z. Xu, J. Wang, J. Zhang, D. Li, B. Zhang, S. Yang, K. Dai, G. Liu, Novel hoberman sphere design for interlaced Mn_3O_4@CNT architecture with atomic layer deposition-coated TiO_2 overlayer as advanced anodes in Li-ion battery, ACS Appl. Mater. Interfaces 12 (2020) 39282–39292.
[27] G. Ren, Z. Luo, Y. Duan, X. Liu, Z. Yuan, F. Cai, Carbon nanotube@Mn_3O_4 composite as cathode for high-performance aqueous zinc ion battery, J. Alloy. Compd. 898 (2022) 162747.
[28] H.W. Chang, Y.R. Lu, J.L. Chen, C.L. Chen, J.F. Lee, J.M. Chen, Y.C. Tsai, C.M. Chang, P.H. Yeh, W.C. Chou, Nanoflaky MnO_2/functionalized carbon nanotubes for supercapacitors: An in situ X-ray absorption spectroscopic investigation, Nanoscale 7 (2015) 1725–1735.
[29] P. Wang, C. Li, S. Dong, X. Ge, P. Zhang, X. Miao, Z. Zhang, C. Wang, L. Yin, Energy storage: One-step route synthesized Co_2P/Ru/N-doped carbon nanotube hybrids as bifunctional electrocatalysts for high-performance Li–O_2 batteries, Small 15 (2019) 1970157.
[30] E. Saputra, H. Zhang, Q. Liu, H. Sun, S. Wang, Egg-shaped core/shell α-Mn_2O_3@α-MnO_2 as heterogeneous catalysts for decomposition of phenolics in aqueous solutions, Chemosphere 159 (2016) 351–358.
[31] P. Zhang, X. Hui, H. Wang, X. Gao, L. Yin, Porous hollow $ZnCo_2S_4$ nanosheet arrays derived from metal-organic framework as efficient cathode for lithium oxygen batteries, J. Alloy. Compd. 860 (2021) 157656.
[32] L. Luo, H. Huang, Y. Yang, S. Gong, Y. Li, Y. Wang, W. Luo, Z. Li, Nickel and manganese oxide heterostructure nanoparticles supported by carbon nanotube for highly efficient oxygen evolution reaction catalysis, Appl. Surf. Sci. 575 (2022) 151699.
[33] Y. Chu, L. Guo, B. Xi, Z. Feng, F. Wu, Y. Lin, J. Liu, D. Sun, J. Feng, Y. Qian, Embedding MnO@Mn_3O_4 nanoparticles in an N-doped-carbon framework derived from Mn-organic clusters for efficient lithium storage, Adv. Mater. 30 (2018) 1704244.
[34] A. Chatterjee, S.W. Or, Metal–organic framework-derived MnO/$CoMn_2O_4$@N–C nanorods with nanoparticle interstitial decoration in core@shell structure as improved bifunctional electrocatalytic cathodes for Li-O_2 batteries, Electrochim. Acta 338 (2020) 135809.
[35] Q. Tan, X. Li, B. Zhang, X. Chen, Y. Tian, H. Wan, L. Zhang, L. Miao, C. Wang, Y. Gan, Valence engineering via in situ carbon reduction on octahedron sites Mn_3O_4 for ultra-long cycle life aqueous Zn-ion battery, Adv. Energy Mater. 10 (2020) 2001050.
[36] Z. Li, K. Song, K. Wang, L. Chen, D. Wei, Y. Lv, Y. Yu, B. Yang, L. Yuan, X. Hu, Fabrication of carbon cloth supporting MnO_x and its application in Li-O_2 batteries, Nanotechnology 31 (2020) 165709.
[37] Z. Qi, A. Younis, D. Chu, S. Li, A facile and template-free one-pot synthesis of Mn_3O_4 nanostructures as electrochemical supercapacitors, Nano-Micro Lett. 8 (2016) 165–173.
[38] F. Wang, M. Xiao, X. Ma, S. Wu, M. Ge, X. Yu, Insights into the transformations of Mn species for peroxymonosulfate activation by tuning the Mn_3O_4 shapes, Chem. Eng. J. 404 (2021) 127097.
[39] H. Zhang, D. Yang, T. Ma, H. Lin, B. Jia, Flash-induced ultrafast production of graphene/MnO with extraordinary supercapacitance, Small Methods 5 (2021) 2100225.

[40] K. Krishnasamy, K. Purushothaman, Preparation and characterisation of $MnS@Mn_3O_4$/C nanoflakes for hybrid supercapacitor applications, Mater. Technol. 37 (2022) 63–70.
[41] P. Wang, C. Li, S. Dong, X. Ge, P. Zhang, X. Miao, R. Wang, Z. Zhang, L. Yin, Hierarchical $NiCo_2S_4$@NiO core–shell heterostructures as catalytic cathode for long-life Li-O_2 batteries, Adv. Energy Mater. 9 (2019) 1900788.
[42] X. Mu, Y. Liu, X. Zhang, H. Wei, P. He, H. Zhou, Using a heme-based nanozyme as bifunctional redox mediator for Li-O_2 batteries, Batteries Supercaps 3 (2020) 336–340.
[43] X. Lin, T. Zhang, C. Chu, Z. Li, R. Liu, P. Li, Y. Li, Z. Huang, Y. Ma, Synthesis of ZIF-derived CoS_2 nanocages interconnected by CNTs for rechargeable Li-O_2 batteries, ACS Sustain. Chem. Eng. 8 (2020) 7581–7587.
[44] P. Wang, C. Li, S. Dong, X. Ge, P. Zhang, X. Miao, Z. Zhang, C. Wang, L. Yin, One-step route synthesized Co_2P/Ru/N-doped carbon nanotube hybrids as bifunctional electrocatalysts for high-performance Li-O_2 batteries, Small 15 (2019) 1900001.
[45] X. Liu, L. Zhao, H. Xu, Q. Huang, Y. Wang, C. Hou, Y. Hou, J. Wang, F. Dang, J. Zhang, Tunable cationic vacancies of cobalt oxides for efficient electrocatalysis in Li-O_2 batteries, Adv. Energy Mater. 10 (2020) 2001415.
[46] Y. Ma, L. Wei, Y. Gu, J. Hu, Y. Chen, P. Qi, X. Zhao, Y. Peng, Z. Deng, Z. Liu, High-performance Li-O_2 batteries based on all-graphene backbone, Adv. Funct. Mater. 30 (2020) 2007218.
[47] J. Li, C. Shu, C. Liu, X. Chen, A. Hu, J. Long, Rationalizing the effect of oxygen vacancy on oxygen electrocatalysis in Li-O_2 battery, Small 16 (2020) 2001812.
[48] M. Mushtaq, X. Guo, Y. Wang, L. Hao, Z. Lin, H. Yu, Composite cathode architecture with improved oxidation kinetics in polymer-based Li-O_2 batteries, ACS Appl. Mater. Interfaces 12 (2020) 30259–30267.
[49] S. Zhang, G. Wang, J. Jin, L. Zhang, Z. Wen, Coupling solid and soluble catalysts toward stable Li anode for high-performance Li-O_2 batteries, Energy Storage Mater. 28 (2020) 342–349.